

Noble metal nanoparticle-functionalized ZnO nanoflowers for photocatalytic degradation of RhB dye and electrochemical sensing of hydrogen peroxide

Muhammad Hussain · Hongyu Sun · Shafqat Karim · Amjad Nisar · Maaz Khan · Anwar ul Haq · Munawar Iqbal · Mashkoor Ahmad

Received: 21 May 2015 / Accepted: 18 March 2016 / Published online: 6 April 2016
© Springer Science+Business Media Dordrecht 2016

Abstract Flower-like hierarchical Zinc oxide nanostructures synthesized by co-precipitation method have been hydrothermally functionalized with 8 nm Au NPs and 15 nm Ag nanoparticles. The photocatalytic and electrochemical performance of these structures are investigated. XPS studies show that the composite exhibits a strong interaction between noble metal nanoparticles (NPs) and Zinc oxide nanoflowers. The PL spectra exhibit UV emission arising due to near band edge transition and show that the reduced PL intensities of Au–ZnO and Ag–ZnO composites are responsible for improved photocatalytic activity arising due to increase in defects. Moreover, the presence of Au NPs on ZnO surface remarkably enhances photocatalytic activity as compared to Ag–ZnO and pure ZnO due to the higher

catalytic activity and stability of Au NPs. On the other hand, Ag–ZnO-modified glassy carbon electrode shows good amperometric response to hydrogen peroxide (H_2O_2), with linear range from 1 to 20 μM , and detection limit of 2.5 μM ($\text{S/N} = 3$). The sensor shows high and reproducible sensitivity of 50.8 $\mu\text{A cm}^{-2} \mu\text{M}^{-1}$ with a fast response less than 3 s and good stability as compared to pure ZnO and Au–ZnO-based sensors. All these results show that noble metal NPs-functionalized ZnO base nanocomposites exhibit great prospects for developing efficient non-enzymatic biosensor and environmental remediators.

Keywords Zinc oxide · Nanostructure · Sensor

Introduction

Metal oxide-based three-dimensional (3D) nanostructures have attracted much interest due to their unique

Electronic supplementary material The online version of this article (doi:10.1007/s11051-016-3397-y) contains supplementary material, which is available to authorized users.

M. Hussain · S. Karim · A. Nisar · M. Khan · M. Ahmad (✉)
Nanomaterials Research Group, Physics Division, PINSTECH, Islamabad 44000, Pakistan
e-mail: mashkoorahmad2003@yahoo.com

H. Sun
Laboratory of Advanced Materials and The State Key Laboratory of New Ceramics and Fine Processing, Department of Materials Science and Engineering Beijing, National Center for Electron Microscopy, Tsinghua University, Beijing, China

H. Sun
Department of Micro- and Nanotechnology, Technical University of Denmark, 2800 Kongens Lyngby, Denmark

A. ul Haq
Non-destructive testing Group, PINSTECH, Islamabad 44000, Pakistan

M. Hussain · M. Iqbal
Centre for High Energy Physics, University of the Punjab, Lahore 54590, Pakistan

properties and enormous applications in the field of optoelectronics, energy, biomedical, and catalysis (Han et al. 2008; Zhou et al. 2011; Liu et al. 2010). Stimulated by these applications, significant advances have been made to design various kinds of metal oxide-based 3D complex hierarchical nanostructures. Such hierarchical architectures combining the features of nanoscale building blocks will show unique properties different from those of the mono-morphological structures. Thus a high degree of complexity of these structures has widened the application window in the bottom-up approaches for the fabrication of functional devices including photocatalysis, solar cells, sensors, and energy harvesting by inheriting the properties of low-dimensional nanostructured building blocks (Hong et al. 2010).

Among the most extensively studied metal oxides, semiconductors photocatalysts Zinc oxide (ZnO), with wide band gap (3.37 eV) and large exciton binding energy (~ 60 meV), has attracted much attention due to its intrinsic electronic properties, photosensitivity, and stability (Jang et al. 2006; Guangbo et al. 2016). Also, ZnO nanostructures present as one of the most promising materials for the fabrication of efficient electrochemical sensors due to having exotic and versatile properties including biocompatibility, non-toxicity, chemical and photochemical stability, high specific surface area, electrochemical activities, high electron communicating features, and so on (Ahmad et al. 2010; Kang et al. 2005). However, some limitations have been found to achieve high photocatalytic efficiency and to enhance electrochemical sensing performance. For example, in photocatalysis, the rapid recombination of carriers limits the photocatalytic efficiency.

ZnO-based composite materials have recently aroused much interest and have been applied in various fields due to their excellent optical, chemical, electronic, mechanical, and thermal properties (Ahmad et al. 2011). These materials also exhibit enhanced electron-transfer kinetics and improved sensing characteristics. The catalytic properties of ZnO have been reported to be enhanced through the incorporation of NPs of conducting or semiconducting materials such as carbon nanotubes, graphene, cobalt, nickel, as well as noble metal NPs (gold, platinum, and silver) with advantages for improved catalytic and sensor characteristics (Li and Wang 2009; Wang et al. 2012; Zeng et al. 2008; Chen et al. 2009). ZnO nanostructures decorated with noble metal NPs have

already found widespread use in a range of applications such as ZnO/Au nanocomposite has been reported for DNA and protein detection, (Liu et al. 2008) ZnO/Ag for photocatalysis (Gu et al. 2009), and ZnO/Pt for Cholesterol detection (Ahmad et al. 2009). Thus noble metal NPs are predicted to serve as a stable electron donor to the conduction band of ZnO.

On the other hand, detection of H_2O_2 has attracted much interest due to its significant use in biotechnology, medicines, food and processing industry, and as a valuable biological marker for many oxidative biological reactions (Lee and John 2006). In addition, it is one of the by-products of glucose oxidation catalyzed by glucose oxidase (GO_x) in the presence of O_2 where the detection of glucose can be achieved on the basis of monitoring the production of H_2O_2 . Therefore, the development of enzymeless sensors is of much importance which provides a multiplex platform for the construction of glucose biosensors (Lu et al. 2011). Enzyme-based sensors have limitations such as instability, stringent operating conditions, complicated immobilization techniques, poisoning of electrodes by adsorbed intermediates, and high cost. Therefore, to overcome these limitations noble metal NPs-ZnO composites have been employed for the fabrication of non-enzymatic electrochemical sensors (Hussain et al. 2014). These nanocomposite-based nanosensors are considered to be a powerful device to detect electroactive species like glucose, hydrogen peroxide.

To realize the demand of these different applications, ZnO nanostructures have been fabricated, including 1D nanorods (Feng et al. 2004) and nanowires (Vayssieres 2003), 2D nanobelts (Arnold et al. 2003) and nanosheets (Kuo et al. 2005), 3D hollow spheres and hierarchically complex architectures. Because of their large surface area and facile mass transport these 3D hierarchical porous nanostructures with large voids are more favorable for sensors, storage, and photocatalysis (Zhao and Jiang 2009). The results prior to our studies have confirmed that the 3D hierarchical structures show superior properties for photocatalysts and water treatment (Ahmad et al. 2011). However, it is still a challenging issue to develop a facile and time-saving method to synthesize 3D hierarchical architectures without using toxic reagents, and functionalize them with noble metals for advanced photocatalytic applications.

Inspired by the need to develop high performance catalysts, highly ordered ZnO were fabricated by

simple co-precipitation chemical method and subsequent hydrothermal incorporation of noble metals (Ag, Au) with these ZnO to significantly improve the catalytic performance.

Experimental section

Reagents

Rhodamine B (RhB) was purchased from ALFA AESAR. $(\text{ZnNO}_3)_2 \cdot 6\text{H}_2\text{O}$ was purchased from RIEDEL-DE HAEN AG SEELZE-HANNOVER; Zn sheet (99.9 %) was purchased from Sinopharm Chemical Reagent Co. Ltd. Chloroauric acid, $\text{AuCl}_3 \cdot \text{HCl} \cdot 3\text{H}_2\text{O}$, KOH, and ethanol (99.8 %) were obtained from MERCK; and AgNO_3 and methanol (99.8 %) were purchased from Sigma Aldrich. All the reagents were of analytical grade and used without further purification. Deionized water was used for the preparation of solutions.

Synthesis of ZnO nanoflowers

Synthesis of hierarchical flower-like ZnO structures were carried out by co-precipitation method similar to as reported previously (Ahmad et al. 2011). In a typical procedure, KOH (4 mol L^{-1}) was prepared by dissolving in 20 mL Deionized water under stirring to form a clear solution. $(\text{Zn}(\text{NO}_3)_2 \cdot 6\text{H}_2\text{O})$ (0.5 mol L^{-1}) solution was also prepared in 20 mL distilled water in a separate beaker. The two solutions were mixed by transfer of $(\text{Zn}(\text{NO}_3)_2 \cdot 6\text{H}_2\text{O})$ solution into KOH solution drop by drop under stirring. Then the final solution was transferred to 50 mL beaker and maintained at room temperature for 24 h; a cleaned piece of Zn sheet as substrate was immersed into the beaker to get the product. After the completion of the reaction, the substrate was washed with distilled water and absolute ethanol several times, and then dried at 85°C for several hours.

Functionalization of ZnO nanoflowers with noble metal nanoparticles

For synthesis of Au decorated ZnO, 1 mL of 0.01 molar $\text{AuCl}_3 \cdot \text{HCl} \cdot 3\text{H}_2\text{O}$ aqueous solution, 3 mL of methanol, and 8 mL of deionized water were mixed in a beaker under stirring. The pH of the solution was

adjusted to 7.5 by adding 0.01 M NaOH. The resulting solution was transferred to 16 mL Teflon-lined autoclave. Zn sheet with ZnO nanoflowers was immersed into the solution and the autoclave was closed tightly and placed into an electric oven at 120°C for 1 h. After cooling down to room temperature, the Zn sheet was rinsed with distilled water and ethanol, and dried at 70°C for 5 h. The same procedure was adopted for Ag decorated-ZnO nanoflowers using 0.01 molar AgNO_3 in 9 mL of ethanol. All other conditions were same except the reaction temperature which was kept at 160°C for 3 h.

Apparatus

Phase purity of the product was analyzed using Rigaku (Dmax III A) X-ray diffractometer (XRD) using $\text{Cu K}\alpha$ ($\lambda = 1.54178 \text{ \AA}$) irradiation. Morphological and microstructural measurements were carried out by the field emission scanning electron microscopy (FESEM-6301F), transmission electron microscopy (TEM, Tecnai G20), and high-resolution transmission microscopy HRTEM by JEM-2011F. Xenon lamp as UV source (PerfectLight, PLS-SXE 300/300UV) and UV-Vis absorption spectra were recorded on Ocean Optics UV-Vis spectrometer (HR2000CG). Electrochemical measurements were performed on Electrochemical Work Station (CHI660e). The Photoluminescence (PL) was performed by Photoluminescence system (Photon Systems Inc. USA). Structural and compositional analysis was examined via X-ray photoemission spectroscopy (XPS) using Super ESCA beam at Elettra, Trieste Italy.

Photocatalytic measurements

Aqueous solution of an organic dye RhB was used as probe to investigate the photocatalytic activity. Pyrex glass vessel was used as photo reactor. The reaction suspensions were prepared by adding 25 mg of each product into three reaction vessels containing 50 mL of $10 \mu\text{molar}$ RhB aqueous solutions. The suspensions were exposed to UV irradiation using 300 W Xenon lamp 30 cm apart from the source. Suspensions were stirred continuously during UV irradiation. Heat produced in the reaction environment was dissipated by forced convection using electric fan. Prior to irradiation, the suspensions were sonicated for 10 min and then stirred magnetically for 30 min in the dark to attain the adsorption-desorption equilibrium of RhB

in the presence of catalyst. Before UV exposure, a 3-mL sample from every solution was taken as a reference. After initiation of the reaction by irradiation, a 3-mL sample of the suspension was taken out at regular intervals and centrifuged to completely remove the catalyst, and UV–Vis absorption spectra were recorded to ensure the RhB photodegradation.

Fabrication of modified GCE as H₂O₂ sensor

Prior to fabrication of H₂O₂ sensor, the Glossy carbon electrodes (GCE) were polished in alumina powder followed by thoroughly sonicating with ethanol, acetone, and water, respectively, and then modified with Au–ZnO and Ag–ZnO nanoflowers. 5 mg of each material (Au–ZnO and Ag–ZnO) were separately mixed ultrasonically with 100 μM Nafion solution for 10–15 min to prepare uniform solutions. 1 μL of these solutions were dropped on the GCE to prepare Nafion/Au–ZnO/GCE and Nafion/Ag–ZnO/GCE-modified electrodes and dried at 50 °C for 30 min. Nafion/ZnO/GCE electrode was also prepared separately for comparison using the same procedure.

Electrochemical measurement

The electrochemical experiments were performed at room temperature utilizing an electrochemical workstation (CHI660e) with a three-electrode configuration. A modified glassy carbon electrode (3 mm in diameter) was used as the working electrode, with Hg/Hg₂SO₄ as the reference electrode, and platinum as the counter electrode. Cyclic voltammetry (CV) was performed in the potential range of $-0.1 + 0.2$ V at a scan rate of 50 mV/s, and amperometric response was carried out at -0.45 V in 0.05 M PBS at 7.2 pH.

Results and discussion

Structural and morphological analysis

The phase of the as-grown and functionalized samples were analyzed by XRD. Figure 1 shows a typical XRD pattern of pure ZnO, Au–ZnO, and Ag–ZnO samples. The pattern shows that all the main diffraction peaks are indexed to wurtzite (hexagonal) ZnO (JCPDS # 00-036-1451) with lattice constants $a = 3.25$ Å and $c = 5.21$ Å. The reflections were at 38.5°, 44.15°, and

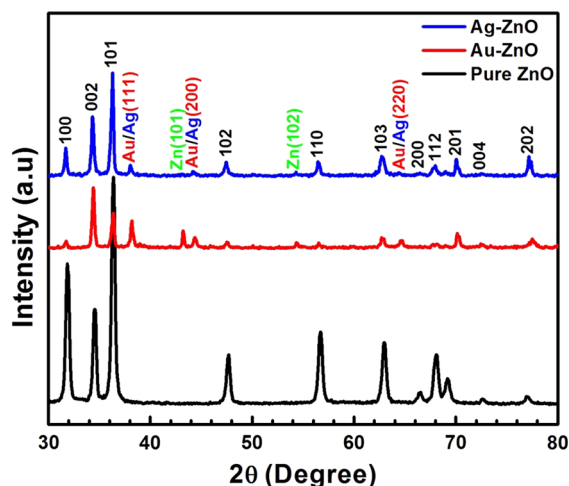


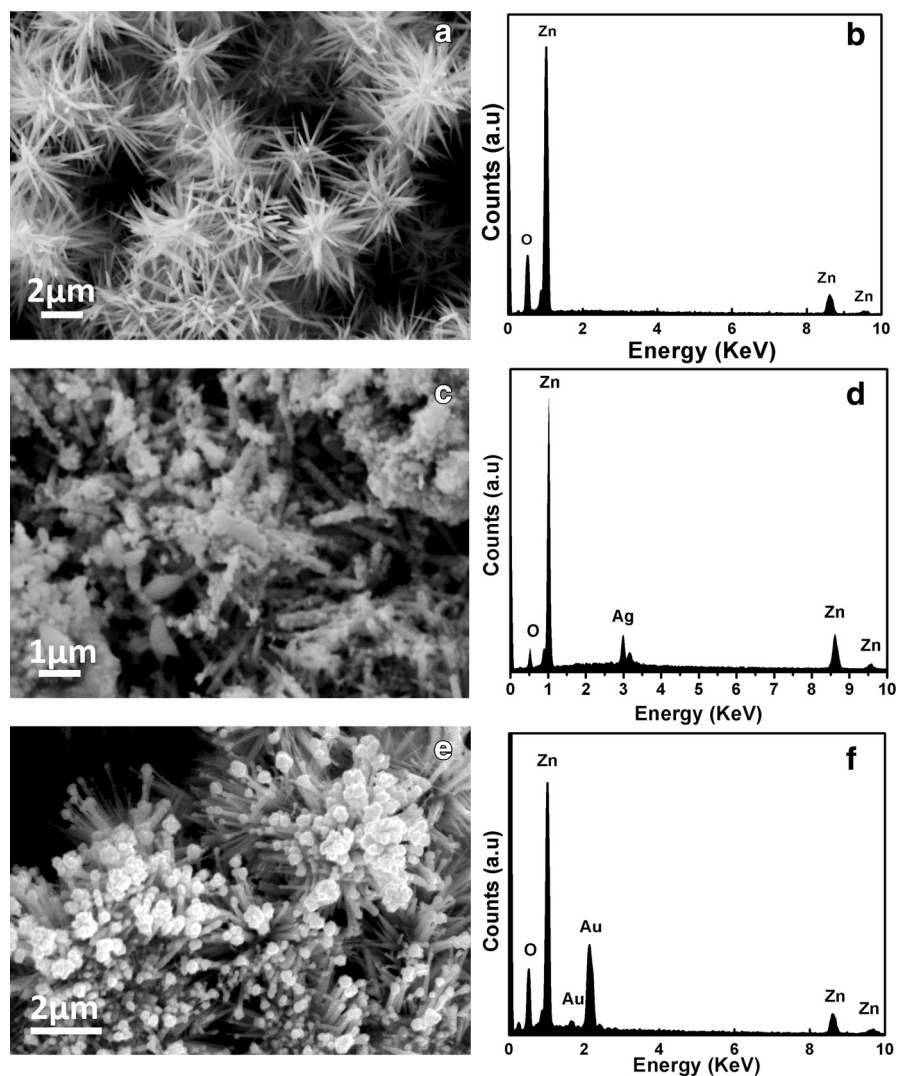
Fig. 1 XRD pattern of Pure ZnO, Ag–ZnO, and Au–ZnO nanostructures

64.45° corresponding to planes (111), (200), and (220), respectively, of face-centered cubic (fcc) Au (JCPDS # 00-002-1095) and Ag (JCPDS # 00-004-0783). Also the diffraction peaks at 43.2° and 54.3° in Au–ZnO and Ag–ZnO pattern corresponding to (101) and (102) are due to the Zn (JCPDS # 00-001-1244) substrate used for collection of products. No other phases are observed in the pattern.

Figure 2a shows the low-magnification SEM image of pure ZnO and illustrates that the product mostly comprises large number of hierarchically flower-like structures. A closed view shows that these flower structures are composed of an array of oriented thorn-like branched nanowires (NWs) with diameter in the range of 50–90 nm and length in the range of microns. Figure 2b shows the corresponding EDS analysis of pure ZnO. Figure 2c, e shows SEM images of flower-like Ag–ZnO and Au–ZnO hybrid nanocomposites, respectively, which demonstrate the deposition of noble metal NPs on the surface of ZnO. It shows that the pure ZnO retain their original structure even after deposition of NPs. It also clearly demonstrates that Ag NPs are agglomerated and deposited in a large amount covering substantially the whole surface of the pure ZnO. The agglomeration of Au NPs is relatively low as compared with Ag NPs. The corresponding EDS patterns of Fig. 2c, e are shown in Fig. 2d, f respectively.

The detailed microstructure and compositional analyses were performed by TEM and HRTEM as

Fig. 2 FESEM image of **a** pure ZnO, **c** Ag-ZnO, and **e** Au-ZnO nanoflowers; corresponding EDS spectrums of **b** pure ZnO, **d** Ag-ZnO, and **f** Au-ZnO nanoflowers



shown in Fig. 3. The TEM image of pure ZnO is shown in Fig. 3a which confirms the flower-like morphology with diameter about 4 μm. The corresponding HRTEM image depicted in Fig. 3b shows the single crystalline wurtzite ZnO NWs. The inter-layer fringe spacing is measured to be 0.24 nm which corresponds to (101) planes of wurtzite ZnO. The TEM images of ZnO, after decoration with Ag and Au NPs, are shown in Fig. 3c, e respectively. It shows that the Ag and Au NPs with average diameter in the range of 2–14 nm and 5–20 nm, respectively, cover most of the surface area of the wires. HRTEM images taken from the segments of Ag-ZnO and Au-ZnO are shown in Fig. 3d, f. The arrows in Fig. 3d, f show the

deposited Ag and Au NPs, respectively. The size distribution of Au and Ag NPs is shown in the insets of Fig. 3d, f.

XPS analysis

To determine the surface composition, oxidation state and the charge transfer tendency between the ZnO, Ag, and Au NPs, XPS studies were also carried out at 1200 eV as shown in Fig. 4. The survey spectra of pure ZnO, Au-ZnO, and Ag-ZnO are shown in supporting information (Fig. S1). It represents Zn 2p, O 1s, Ag 3d, and Au 4f oxidation peaks confirming the presence of Zn, Au, Ag, and O in the composite and no

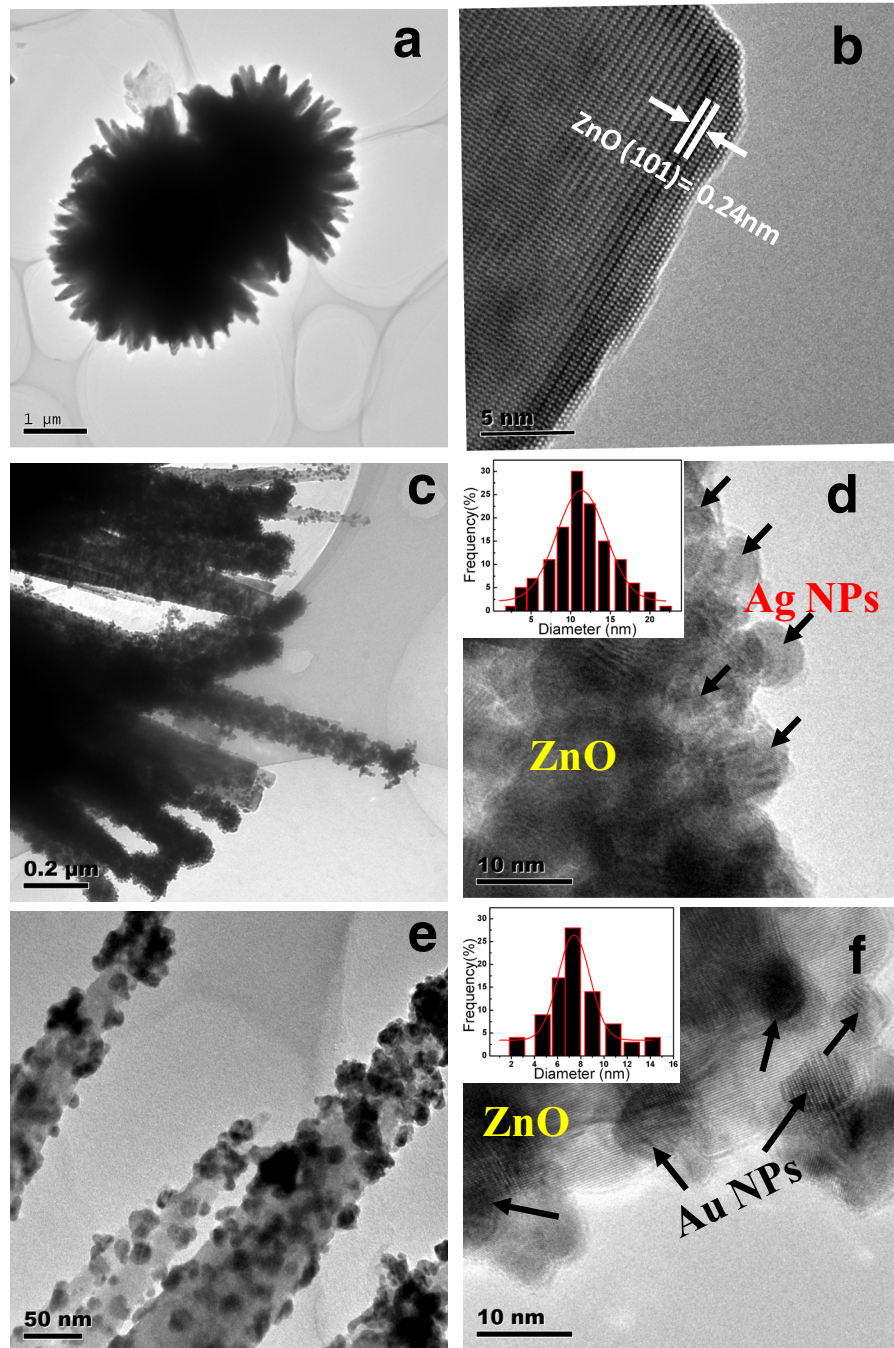


Fig. 3 **a** Low-magnification TEM image of pure ZnO nanoflowers. **b** HRTEM image of a part of single wire taken from **a**, **c** low-magnification TEM image of Ag-ZnO and **d** corresponding high-magnification image of Ag-ZnO, **e** low-

magnification TEM image of Au-ZnO and **f** corresponding high-magnification image of Au-ZnO. *Inset* in **d** and **f** is the size distribution of Ag and Au NPs dispersed on the pure ZnO surface

peaks of any other elements are observed. Figure 4a shows typical high-resolution spectra of Zn2P peak of the three samples, which exhibit two significant

binding energy peaks at 1023.18 and 1046.34 eV corresponding to the electronic states of Zn2p_{5/2} and Zn2p_{3/2}, respectively. The binding energy peaks of

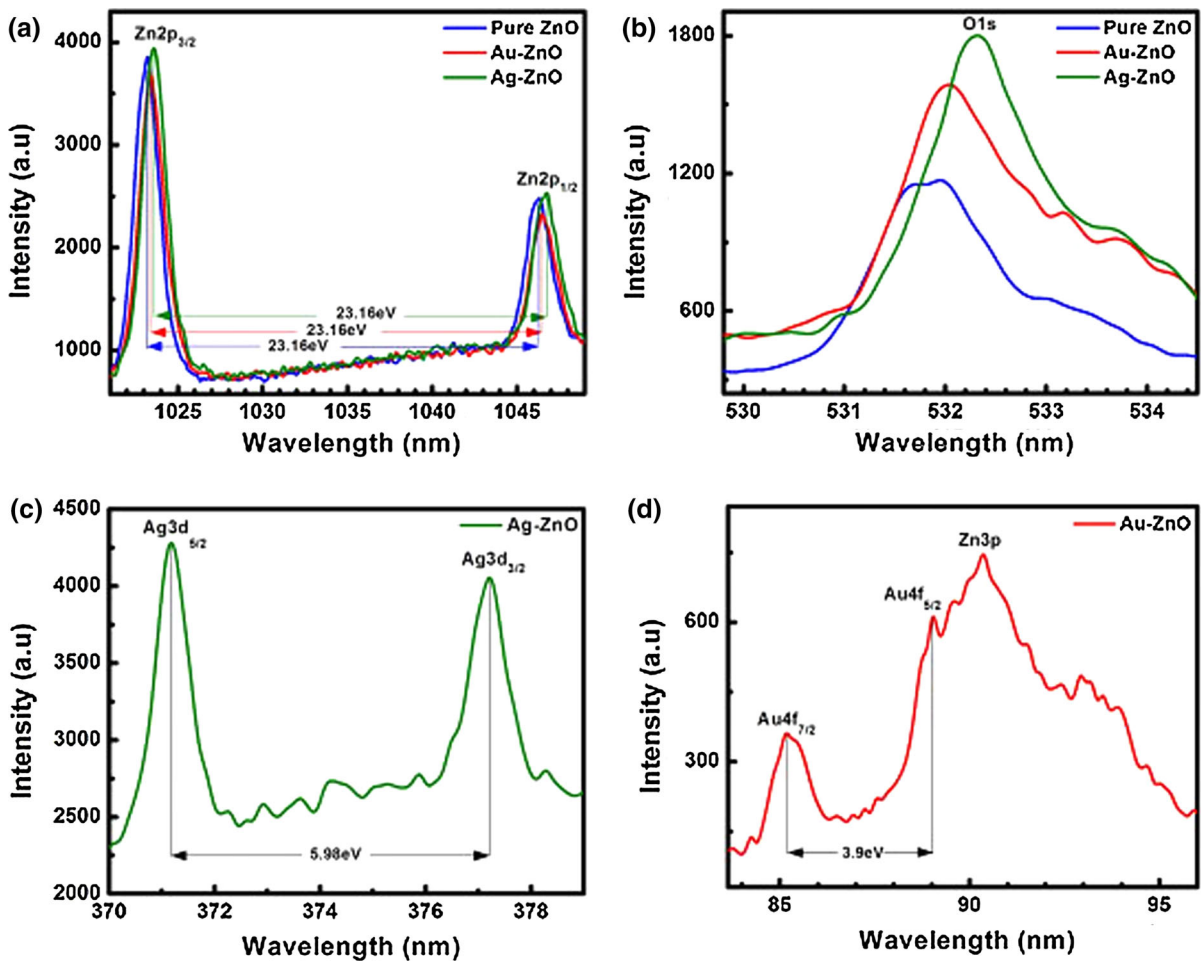


Fig. 4 XPS spectra of **a** Zn2p for pure ZnO, Au–ZnO, and Ag–ZnO, **b** O1s **c** Ag3d, and **d** Au4f

composites shift toward higher binding energy as compared to pure ZnO due to strong interaction between metallic Au, Ag NPs, and ZnO (Wang et al. 2013). Moreover, the energy difference between the two peaks for all the three samples is 23.16 eV which agrees well with the standard values of 23.0 eV (Wagner 1979); the high-resolution O1s XPS spectra of the three samples are shown in Fig. 4b. It can be seen that O1s oxidation peaks are somewhat asymmetric indicating the existence of two kinds of oxygen species on the samples surface (Lu et al. 2008). The oxidation peaks located at 531.97, 532.12, 532.27 eV correspond to binding energies of pure ZnO and functionalized with Au and Ag NPs, respectively. This exhibits positive shift compared to bulk ZnO which is attributed to surface hydroxyl oxygen (O–OH). The shoulder peak toward higher binding energy sides of

the three samples indicate the presence of surface hydroxyl groups or chemisorbed water molecules (Nagaveni et al. 2004). Figure 4c shows the high-resolution XPS spectrum of Ag3d peak in the composite. It exhibits two peaks located at 371.25 and 377.23 eV corresponding to Ag 3d_{5/2} and Ag 3d_{3/2}. Compared to bulk Ag (368.3 eV for Ag 3d_{5/2} and 374.3 eV for Ag 3d_{3/2}), an obvious positive shift is observed which further indicates that some electrons may migrate from the ZnO to metallic Ag, and there is a strong interaction between the Ag NPs and ZnO support. The AgNPs can act as electron acceptors and help to separate the photoexcited electron–hole pairs. The energy difference between the two states is 5.98 eV which is close to the bulk value of 6 eV as reported by Wagner et al. The high-resolution Au4f spectra along with Zn2p peak are indicated in Fig. 4d.

It represents significant binding energies at 85.14 and 89.02 eV corresponding to Au4f_{7/2} and Au4f_{5/2}. This shows that gold is only present in metallic form in the Au–ZnO composite. An interference peak at 89.06 eV is also appeared due to Au4f_{5/2} along with Zn3p peak. A close observation shows that binding energy of Au 4f_{7/2} exhibits a positive shift in comparison to 83.8 eV of bulk Au, which is probably caused by electron transfer from plasmonic Au NPs to ZnO due to the strong electronic interaction between AuNPs and oxide support. Further, the binding energy of Au 4f_{5/2} exhibits a positive shift due to overlapping by the interference of Zn 3p peak (Liu et al. 2011; Wang et al. 2009a, b). The difference in the energy shift may either be due to the ZnO support and Au/Ag NPs or the interaction between the oxygen species and the noble metal NPs due to the oxygen available in the hydrothermal reaction. Since no such peaks other than Au4f are observed in the spectrum, it illustrates that Au exists in pure metallic form. Hence, there is a strong possibility of charge transfer between Au and ZnO support providing/giving the greater tendency to Au of capturing the electrons from the ZnO (Wang et al. 2013). Moreover, the energy difference between the two peaks is 3.9 eV, which agrees well with the standard value of 3.7 eV.

Optical properties

The room-temperature PL spectra of pure ZnO, Au-, and Ag-deposited ZnO NPs are shown in Fig. 5. It is found that all the three samples show UV emission band at 380 nm arising due to near band edge transition, and is ascribed to the recombination of free excitons between the near band edge transitions of the wide band gap of noble metal NPs decorated ZnO nanocomposites. This demonstrates that functionalizing of Au and Ag NPs with the ZnO nanoflowers does not give rise to new PL phenomena. Moreover, it can be observed from the figure that the PL intensities of Au–ZnO and Ag–ZnO composites are lower than that of pure ZnO. This indicates that the deposited Au and Ag NPs has the tendency to hinder the recombination of photo-induced electrons and holes and can act as electron sinks, accounting for the reduced intensity of the PL emission. Because the Au and Ag NPs can act as electron scavengers and help to increase the separation effect of the photo-induced $e^- - h^+$ pairs,

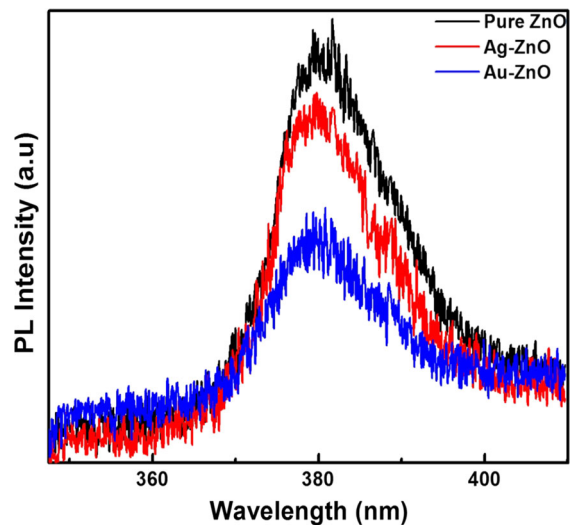


Fig. 5 PL spectra of pure ZnO, Ag–ZnO, and Au–ZnO nanostructures

the hybrid nanocomposites can inhibit the recombination of excited electrons and holes and enhance the photocatalytic activity. This is in good agreement with our XPS data in which the increase in the band gap energy of the noble metal NPs is due to fact that the deposited noble metals have the greater tendency to accept the photogenerated electrons from the ZnO nanoflowers (Lu et al. 2008; Wang et al. 2013).

Photocatalytic performance

Photocatalysis depends upon the excitation of electrons from the valance band to the conduction band of the semiconductor if a light of some suitable energy is incident on it. This process can be efficiently improved if some certain metals are deposited on the semiconductor surface. As the noble metal nanoparticles indirectly influence the interfacial charge transfer process, therefore it is important to consider the possible photo-induced interactions as well as interfacial charge transfer between metal and semiconductor. When light of certain wavelength equal or greater than the band gap of semiconductor falls on the catalyst, it results in the excitation of electrons from valance band to the conduction band leaving behind the same number of holes (h^+) in the valance band. The resulting holes are primarily responsible for the formation of hydroxyl radicals ($\cdot\text{OH}$) which

subsequently degrade the pollutant adsorbed onto the surface of the catalyst.

Actually when noble metal NPs are deposited on the semiconductor surface, metal–semiconductor junction is formed. The Fermi levels of the metal and semiconductor are different due to the difference in their work functions. As the work function of metal is lower than the semiconductor, its Fermi level is higher than the semiconductor. Therefore during the time of metal–semiconductor contact formation, their Fermi levels are aligned by transferring electron from metal to the semiconductor and a common equilibrated Fermi level representing the metal–semiconductor composite is formed. During UV exposure, the electrons move from semiconductor to the metal due to the fact that the conduction band minima of semiconductor is higher than the new equilibrated Fermi level of metal–semiconductor composite (Au–ZnO, Ag–ZnO), the electrons would transfer from semiconductor (ZnO) to the noble metal NPs (Au, Ag) driven by UV irradiation. Hence, the noble metal acts as sink for the excited electrons by capturing and hindering these electrons from recombination with the holes at the VB and releases the electrons in the solution which react with the dissolved oxygen to form super oxide ions ($\bullet\text{O}_2^-$) eventually forming the hydroxyl radicals ($\bullet\text{OH}$). The holes at the VB also react with the water to form $\bullet\text{OH}$. Ultimately, both electrons and holes generate the hydroxyl radicals which are very oxidative in nature and react with the organic dye molecules to degrade it into CO_2 and H_2O .

The photocatalytic performance of the noble metal-incorporated ZnO nanostructures was measured by photo degradation of a well-known organic dye RhB, under UV light irradiation. Initially, absorption spectrum (supporting Fig. S2) of RhB aqueous solution (initial concentration, 10 μM , 50 mL) without any photocatalyst obtained by irradiating with UV lamp and 3 ml of irradiated solution was taken after equal intervals of time. The absorption peak corresponding to RhB molecule at 561 nm decreases slowly with the increasing exposure time and reduces about 20 % of its original value after the 60 min irradiation. Comparative experiments were carried out to investigate the photocatalytic activity of as-grown ZnO (Fig. 6a), Ag–ZnO (Fig. 6b), and Au–ZnO (Fig. 6c) using 25 mg of each material in the same RhB concentration. The corresponding absorption spectra as a

function of degradation time are shown in Fig. 6. Figure 6a shows that that absorption peak of RhB molecule vanishes after 30 min of UV exposure in the presence of pure ZnO as catalyst. But the degradation time reduces to 14 and 10 min for Ag and Au NPs-functionalized ZnO nanocomposite as shown in Fig. 6b and c, respectively. It demonstrates that the degradation of RhB for noble metal-functionalized ZnO is much higher than the pure ZnO.

Figure 6d shows the comparison of the time profiles of the decrease in RhB concentration in the absence and in the presence of different photocatalysts. The blank experiment shows that the photodegradation of RhB alone is insignificant. It should be noted that pure ZnO shows observable photocatalytic activity under UV irradiation, but with rather slow kinetics. The presence of Au–ZnO reduces the dye concentration up to 99 % within 10 min as compared to RhB blank, pure ZnO, and Ag–ZnO whose degradation efficiency is 89 % for the same period of time. There may be the following reasons that make Au–ZnO more efficient photocatalyst than Ag–ZnO. The catalytic efficiency of noble metal composite is related to (1) the defects introduced, unintentionally or deliberately, into the nanomaterials during the synthesis and (2) the total density of the noble metal nanoparticles on the semiconductor nanostructure surface. The nanomaterials with more oxygen-related defects are more efficient photocatalysts (Zheng et al. 2008). The NPs act as electron sinks during the photogeneration of electrons. It provides sites for photogenerated electrons and holes, and delays the recombination of these photoseparated carriers. Moreover, the higher surface loading of the metal contents decreases the photocatalytic efficiency of the semiconductor due to reductive availability of the semiconductor for light absorption and pollutant adsorption (Lu et al. 2008). In aspect of the above reasons, the photocatalysis of Au–ZnO and Ag–ZnO are in accordance with the literature and in good agreement with PL and HRTEM images as shown in Fig. S3. Hence the results demonstrate that the presence of Au–ZnO composite induces significant improvement in the photo-degradation efficiency due to large surface area and specific morphology. It has been found that the values reported in this finding show relatively higher activity than that reported earlier (Ahmad et al. 2011; Lu et al. 2008). The

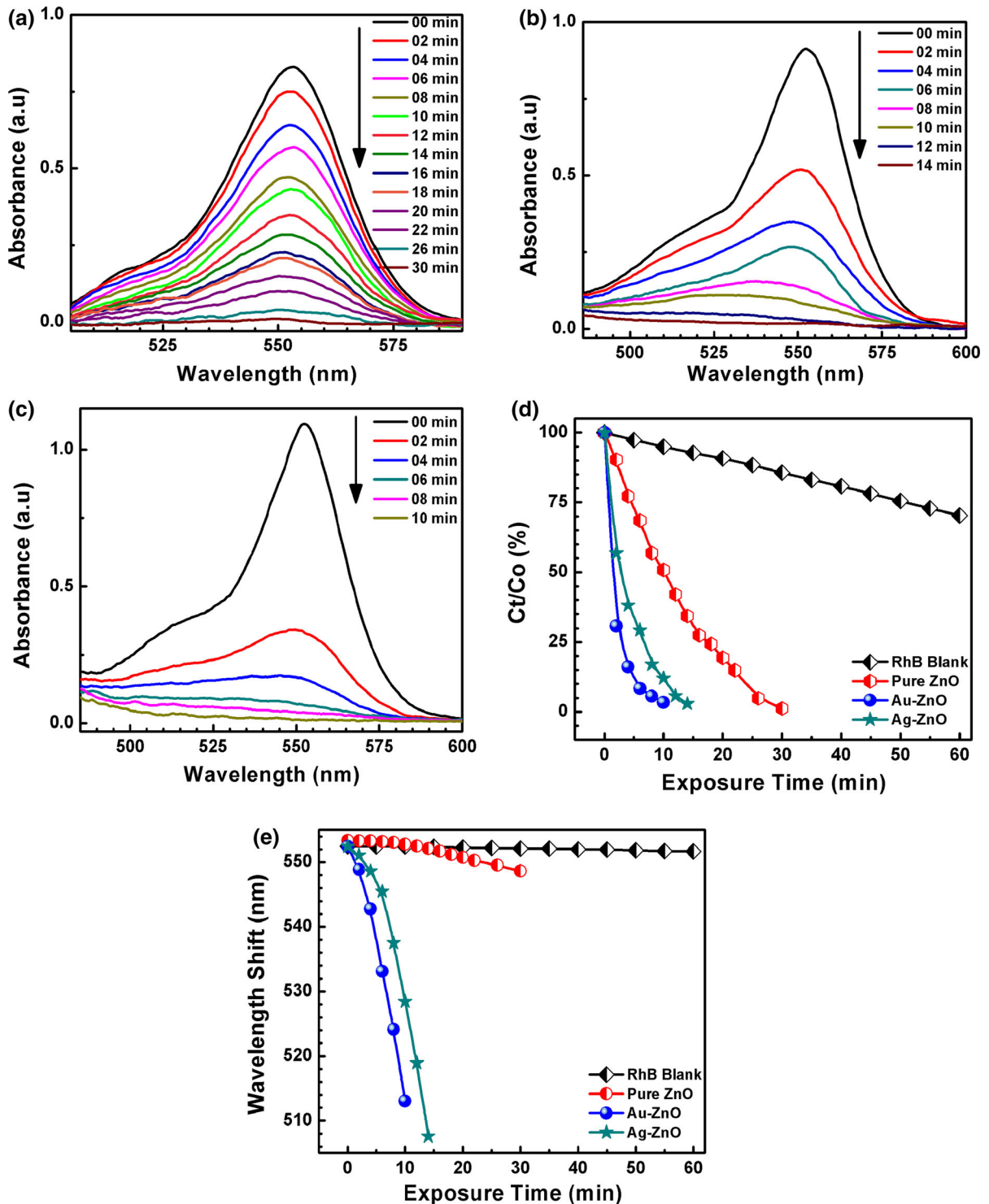


Fig. 6 Time-dependent UV-Vis spectral changes of RhB aqueous solution in the presence of **a** pure ZnO, **b** Ag-ZnO, and **c** Au-ZnO, **d** photocatalytic degradation curves (Ct/Co vs T) of RhB without the presence of any catalyst (RhB blank) and

in the presence of pure ZnO, Ag-ZnO, and Au-ZnO upon UV exposure, **e** wavelength shift of the spectra of RhB solution in the presence of pure ZnO, Ag-ZnO, and Au-ZnO and in the absence of any type of photocatalyst (RhB blank)

Table 1 Photocatalytic degradation of 10 μM RhB using nanostructures as photocatalysts synthesized by different techniques

Structure	Synthesis tech	Temp($^{\circ}\text{C}$)	Dye	Source	Deg. time(min)	References
Flower-like Au–ZnO	HT, ECD	RT	RhB	UV	90	Vayssieres (2003)
Ag/ZnO hollow Sp	HT	RT	RhB	UV	50	Wang et al. (2009a)
ZnO/Au hybrid NS	HT, sorption	RT	RhB	UV	15	[Wang et al. 2009b]
Pt/ZnO nanocages	Las. ablation	RT	RhB	UV	40	[Zeng et al. 2008]
Flower-like ZnO	Co-precip.	RT	RhB	UV	100	[Li and Wang 2009]
Ag–ZnO N flowers	HT, Co-precip.	RT	RhB	UV	14	Present work
Au–ZnO N flowers	HT, Co-precip.	RT	RhB	UV	10	Present work
ZnO N flowers	Co-precip.	RT	RhB	UV	30	Present work

comparison of photocatalytic characteristics of various ZnO-based nanostructures is shown in Table 1. The increase in UV irradiation time leads to the changes in wavelength of the complex dye molecule. The decrease in absorption wavelength as a function of UV exposure time is shown in Fig. 6e. It shows that the dye molecule is de-ethylated showing blue shift in the spectrum (Hussain et al. 2014). The efficiency and stability of the catalyst are also observed by performing three cycles of operation. The time profile of the change in concentration of RhB aqueous solution for the three cycles in the presence of Au–ZnO and Ag–ZnO photocatalyst can be observed in the Fig. S4. It can be clearly seen that the Au–ZnO photocatalyst is more stable and the efficiency does not decrease significantly after three cycles of operation. These results demonstrate that the Au–ZnO can indeed serve as highly effective and convenient recyclable photocatalyst. It was also observed that the morphology of the hybrid nanostructure (not shown here) did not show significant change after three cycles of operation.

Electrochemical measurements

Detection of H_2O_2 by Au–ZnO and Ag–ZnO modified glassy carbon electrodes

To investigate the electrochemical behavior, cyclic voltammetric (CV) sweep curves of the prepared nanostructures were measured in the range from -0.1 to $+0.2$ versus $\text{Hg}/\text{Hg}_2\text{Cl}_2$ at a scan rate of 50 mV/s. The cyclic voltammograms of bare GCE and ZnO, Au–ZnO, and Ag–ZnO-modified GCE in 0.05 M phosphate buffer solution (pH 7.2) before and after addition of 1 μM H_2O_2 are shown in Fig. 7a. It can be

observed that the modified electrodes show small background current in the absence of H_2O_2 . Upon addition of 1 μM H_2O_2 , the CV changed dramatically with pronounced increase of the oxidation current. The electrochemical oxidation of H_2O_2 started at about -0.68 to -0.1 V versus $\text{Hg}/\text{Hg}_2\text{Cl}_2$. It can be noted that in comparison to GCE without the addition of H_2O_2 , the CV response for nafion/Ag–ZnO/GCE is much higher than nafion/ZnO/GCE and nafion/Au–ZnO/GCE. This may be due to the maximum surface covering density of Ag NPs on ZnO which is in good agreement. High surface covering density of Ag NPs on pure ZnO is favorable for H_2O_2 sensing which causes increase in current during the addition of 1 μM H_2O_2 .

Amperometric response

The typical amperometric responses of nafion/ZnO/GCE, nafion/Au–ZnO/GCE, and nafion/Ag–ZnO/GCE-modified electrodes to the varying concentrations of H_2O_2 by successive addition of 1 μM H_2O_2 in the continuously stirred 0.1 M PBS at a working potential of -0.45 V versus $\text{Hg}/\text{Hg}_2\text{Cl}_2$ are shown in Fig. 7b. In comparison to ZnO and Au–ZnO-modified electrodes, Ag–ZnO electrode exhibits rapid and sensitive response to the change in concentration of hydrogen peroxide and the amperometric current is noticeably increased upon successive addition of H_2O_2 . The modified electrode achieved 95 % of the steady state current within less than 3 s which indicates the good oxidative and fast electron exchange behavior of Ag–ZnO. Moreover, the amperometric response of Ag–ZnO modified electrode is higher than that of Au–ZnO. The corresponding calibration curves of all the three modified electrodes

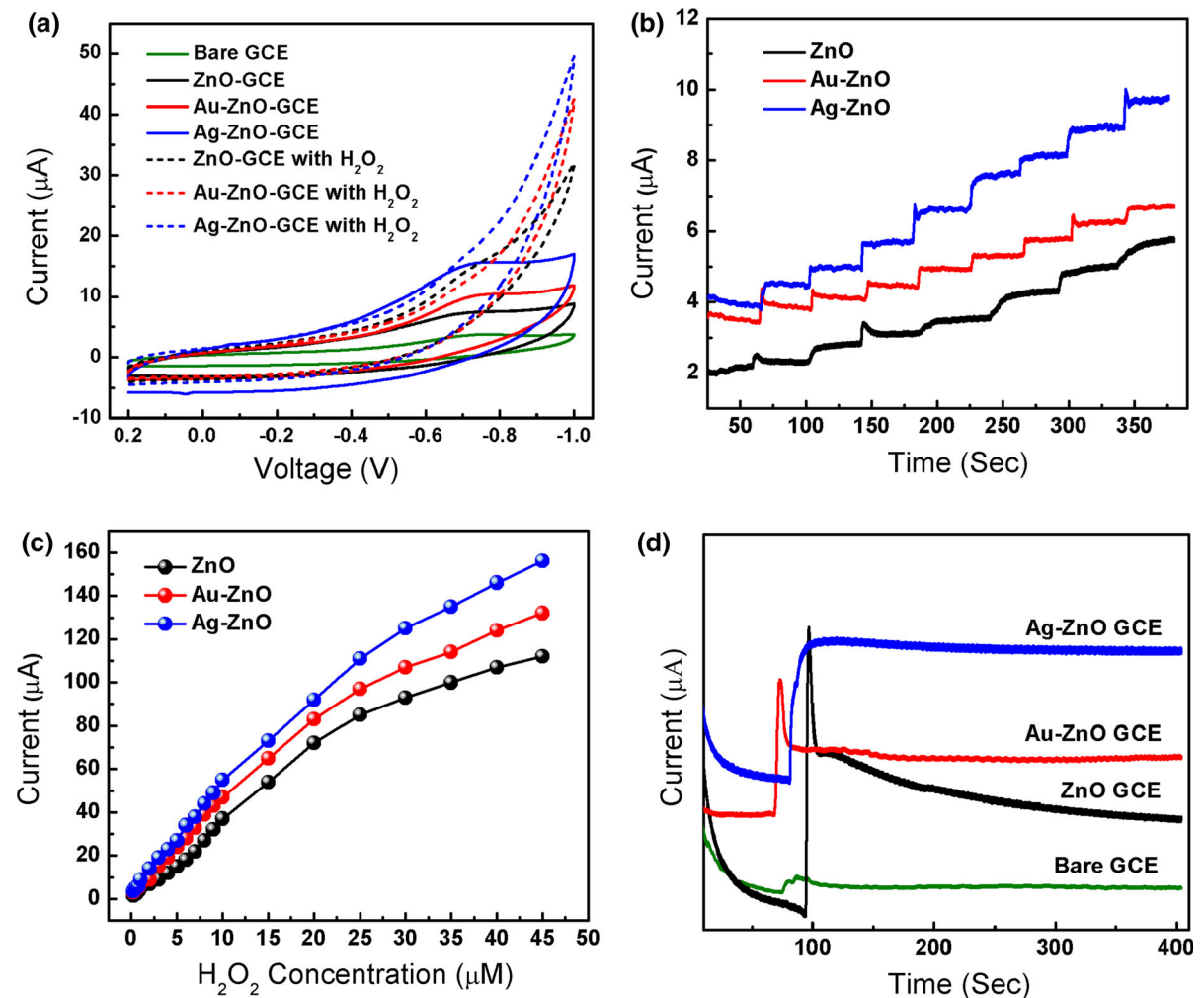


Fig. 7 **a** Cyclic voltammograms of bare and modified GCE with pure ZnO, Au-ZnO, and Ag-ZnO in the absence of H_2O_2 and in the presence of H_2O_2 **b** amperometric response of three modified GCE at constant voltage of -0.45 V with successive

addition of $1 \mu\text{M}$ H_2O_2 in 0.05 M PBS under stirring **c** corresponding calibration curves of the three modified electrodes and **d** stability plot of the three modified GCE at constant potential of -0.45 V in the presence of $1 \mu\text{M}$ H_2O_2

are shown in Fig. 7c. It shows that with the increase in H_2O_2 concentration, the response current increases and tends to approach a saturation value at high concentration. The linear range of calibration curve for these modified electrodes is from 1 to $20 \mu\text{M}$ (correlation factor, $R = -0.998$) with a low limit of detection (LOD) of about $-2.5 \mu\text{M}$. The sensitivity of the H_2O_2 sensor for Ag-ZnO-modified electrode is $50.8 \mu\text{A cm}^{-2} \mu\text{M}^{-1}$, which is much higher than that of Au-ZnO and ZnO-modified electrodes.

The typical amperometric response and stability of the current with the addition of $1 \mu\text{M}$ H_2O_2 under continuous stirring was measured for the modified

electrodes and is shown in Fig. 7d. For comparison, similar measurements were also performed with bare electrode. It is obvious that Ag-ZnO-modified GCE is more stable as compared to Au-ZnO and pure ZnO showing higher value of current with steady state current loss of 1.5% after 300 s. Moreover, Ag-ZnO/GCE is more stable than others with negligible loss in steady current for the same interval of time.

To investigate the fabrication repeatability of the three modified GC electrodes, CV measurements were performed 10 times for each electrode under identical experimental conditions and excellent relative standard deviations (RSD) of 1.57 , 1.74 , and 1.78% were

Table 2 Fabrication repeatability in μA of the three modified GCE

Type of electrode	Times										RSD %
	1st	2nd	3rd	4th	5th	6th	7th	8th	9th	10th	
Ag-ZONFs	50	49.8	48.03	49.02	48.13	50	48.35	48.25	49.1	48	1.57
Au-ZONFs	42	42.1	41.9	41.13	41.5	41.63	41.76	42	41.8	40	1.74
Pure ZONFs	33	31.12	32.5	32.1	32.31	33	32.51	32.11	33	32.67	1.78

achieved for Au-ZnO, Ag-ZnO, and pure ZnO, respectively as shown in Table 2. This shows a good reproducibility of these modified electrodes toward H_2O_2 sensing.

Here, we note that the nanocomposites of Au-ZnO and Ag-ZnO behave differently for photo and biosensing activities. Both of these processes (photocatalysis and biosensing) involve redox reaction but different mechanisms are involved regarding the transportation of charged carriers. Photocatalysis is based on the photo separation and recombination, while the H_2O_2 sensing relies on the transportation of the carriers between the electrodes. In addition, the defects produced in the material after integrating noble metal NPs with the ZnO act as electron sinks which delay the carrier recombination in photocatalysis process and inhibit the ions mobility and transportation during redox in the H_2O_2 sensing. Therefore, according to our PL results Au-ZnO is a good photocatalyst than Ag-ZnO but contrary to this Nafion/Ag-ZnO/GCE has better sensing properties than Nafion/Au-ZnO/GCE-modified electrode.

Conclusions

Flower-like ZnO nanostructures have been successfully functionalized with noble metal NPs and were found to be multifunctional. The photodegradation efficiency of RhB aqueous solution in the presence of Au-ZnO is found to be more prominent than pure ZnO and Ag-ZnO. This improved photocatalytic performance of Au-ZnO composite can be attributed to the defects induced during synthesis. On the other hand, electrochemical measurements show that the noble metal NPs exhibits remarkable catalytic performance toward H_2O_2 detection. Moreover Ag-ZnO modified GCE is found to be more sensitive as compared to pure ZnO and Au-ZnO-modified GC electrode due to fast electron transfer caused by increased density of Ag

NPs on ZnO. Thus Ag-ZnO-modified GCE exhibits excellent performance for H_2O_2 detection with good sensitivity, low detection limit, long-term stability, and repeatability. Hence, noble metal-integrated ZnO nanostructures provide a new platform for applications in photocatalysis and in designing enzymeless biosensors.

Acknowledgments The authors are very thankful to Dr Javed Bashir, Director Science PINSTECH for the financial support through PINSTECH Phase-II project. The authors are thankful to Pakistan Science Foundation and TWAS for financial support through projects [PSF/Res/C-PINSTECH/Phys (172)] and (13-319RG/MSN/AS-C-UNESCO FR:3240279202), respectively. The authors also acknowledge the contribution of Syed Zahid Hussain, Material Division PINSTECH for XRD analysis.

References

- Ahmad M, Caofeng P, Lin G, Zeeshan N, Jing Z (2009) Highly sensitive amperometric cholesterol biosensor based on Pt-incorporated fullerene-like ZnO nanospheres. *J Phys Chem C* 114:243–250. doi:10.1021/jp9089497
- Ahmad M, Caofeng P, Zhixiang L, Jing Z (2010) A single ZnO nanofiber-based highly sensitive amperometric glucose biosensor. *J Phys Chem C* 114:9308–9313. doi:10.1021/jp102505g
- Ahmad M, Shi Y, Amjad N, Hongyu S, Wanci S, Miao W, Jing Z (2011) Synthesis of hierarchical flower-like ZnO nanostructures and their functionalization by Au nanoparticles for improved photocatalytic and high performance Li-ion battery anodes. *J Mater Chem* 21:7723–7729. doi:10.1039/C1JM10720H
- Arnold MS, Phaedon A, Zheng WP, Zhong LW (2003) Field-effect transistors based on single semiconducting oxide nanobelts. *J Phys Chem B* 107:659–663. doi:10.1021/jp0271054
- Chen L, Linbao L, Zhenhua C, Mingliang Z, Juan AZ, Chun SL, Shuit TL (2009) ZnO/Au composite nanoarrays as substrates for surface-enhanced Raman scattering detection. *J Phys Chem C* 114:93–100. doi:10.1021/jp908423v
- Feng X, Lin F, Meihua J, Jin Z, Lei J, Daoben Z (2004) Reversible super-hydrophobicity to super-hydrophilicity transition of aligned ZnO nanorod films. *J Am Chem Soc* 126:62–63. doi:10.1021/ja038636o

- Gu C, Chun C, Haiyou H, Tailun W, Ning W, Tong YZ (2009) Growth and photocatalytic activity of dendrite-like ZnO@Ag heterostructure nanocrystals. *Cryst Growth Des* 9:3278–3285. doi:[10.1021/cg900043k](https://doi.org/10.1021/cg900043k)
- Guangbo C, Yufei Z, Lu S, Geoffrey Waterhouse IN, Xiaofeng K, Li-ZW, Chen-HT and Tierui Z (2016) Recent advances in the synthesis, characterization and application of Zn²⁺-containing heterogeneous catalysts. doi: [10.1002/adv.201500424](https://doi.org/10.1002/adv.201500424)
- Han XG, Hui ZH, Qin K, Xi Z, Xian HZ, Tao XX, Zhao X, Lan SZ (2008) Controlling morphologies and tuning the related properties of nano/microstructured ZnO crystallites. *J Phys Chem C* 113:584–589. doi:[10.1021/jp808233e](https://doi.org/10.1021/jp808233e)
- Hong Y, Xuesi C, Xiabin J, Hongsong F, Bo G, Zhongwei G, Xingdong Z (2010) Preparation, bioactivity, and drug release of hierarchical nanoporous bioactive glass ultrathin fibers. *Adv Mater* 22:754–758. doi:[10.1002/adma.200901656](https://doi.org/10.1002/adma.200901656)
- Hussain M, Mashkoo A, Amjad N, Hongyu S, Shafqat K, Maaz K, Sabih DK, Munawar I, Syed ZH (2014) Enhanced photocatalytic and electrochemical properties of Au nanoparticles supported TiO₂ microspheres. *New J Chem* 38:1424–1432. doi:[10.1039/C3NJ01525D](https://doi.org/10.1039/C3NJ01525D)
- Jang ES, Won JH, Hwang SJ, Choy JH (2006) Fine tuning of the face orientation of ZnO crystals to optimize their photocatalytic activity. *Adv Mater* 18:3309–3312. doi:[10.1002/adma.200601455](https://doi.org/10.1002/adma.200601455)
- Kang BS, Ren F, Heo YW, Tien LC, Norton DP, Pearton SJ (2005) pH measurements with single ZnO nanorods integrated with a microchannel. *Appl Phys Lett* 86:112105. doi:[10.1063/1.1883330](https://doi.org/10.1063/1.1883330)
- Kuo CZ, Kuo TJ, Michael HH (2005) Hydrothermal synthesis of ZnO microspheres and hexagonal microrods with sheetlike and platelike nanostructures. *J Phys Chem B* 109:20115–20121. doi:[10.1021/jp0528919](https://doi.org/10.1021/jp0528919)
- Lee JW, John DH (2006) The PerR transcription factor senses H₂O₂ by metal-catalysed histidine oxidation. *Nature* 440:363–367. doi:[10.1038/nature04537](https://doi.org/10.1038/nature04537)
- Li B, Wang Y (2009) Facile synthesis and enhanced photocatalytic performance of flower-like ZnO hierarchical microstructures. *J Phys Chem C* 114:890–896. doi:[10.1021/jp909478q](https://doi.org/10.1021/jp909478q)
- Liu Y, Mingya Z, Guiye S, Yajun L, Baiqu H, Guoliang Y (2008) Biocompatible ZnO/Au nanocomposites for ultrasensitive DNA detection using resonance Raman scattering. *J Phys Chem B* 112:6484–6489. doi:[10.1021/jp710399d](https://doi.org/10.1021/jp710399d)
- Liu C, Feng L, Lai PM, Hui MC (2010) Advanced materials for energy storage. *Adv Mater* 22:E28–E62. doi:[10.1002/adma.200903328](https://doi.org/10.1002/adma.200903328)
- Liu X, Zhang J, Wang L, Yang T, Guo X, Shihua W, Wang S (2011) 3D hierarchically porous ZnO structures and their functionalization by Au nanoparticles for gas sensors. *J Mater Chem* 21:349–356. doi:[10.1039/C0JM01800G](https://doi.org/10.1039/C0JM01800G)
- Lu W, Shuyan G, Jianji W (2008) One-pot synthesis of Ag/ZnO self-assembled 3D hollow microspheres with enhanced photocatalytic performance. *J Phys Chem C* 112:16792–16800. doi:[10.1021/jp803654k](https://doi.org/10.1021/jp803654k)
- Lu W, Yonglan L, Guohui C, Xuping S (2011) Synthesis of functional SiO₂-coated graphene oxide nanosheets decorated with Ag nanoparticles for H₂O₂ and glucose detection. *Biosens Bioelectron* 26:4791–4797. doi:[10.1016/j.bios.2011.06.008](https://doi.org/10.1016/j.bios.2011.06.008)
- Nagaveni K, Hegde MS, Ravishankar N, Subbanna GN, Giridhar M (2004) Synthesis and structure of nanocrystalline TiO₂ with lower band gap showing high photocatalytic activity. *Langmuir* 20:2900–2907. doi:[10.1021/la035777v](https://doi.org/10.1021/la035777v)
- Vayssieres LL (2003) Growth of arrayed nanorods and nanowires of ZnO from aqueous solutions. *Adv Mater* 15:464–466. doi:[10.1002/adma.200390108](https://doi.org/10.1002/adma.200390108)
- Wagner CD (1979) Handbook of x-ray photoelectron spectroscopy: a reference book of standard data for use in x-ray photoelectron spectroscopy. Perkin-Elmer Corp Physical Electronics Division, Waltham
- Wang C, Daimon H, Shouheng S (2009a) Dumbbell-like Pt – Fe₃O₄ nanoparticles and their enhanced catalysis for oxygen reduction reaction. *Nano Lett* 9:1493–1496. doi:[10.1021/nl8034724](https://doi.org/10.1021/nl8034724)
- Wang Q, Geng B, Wang S (2009b) ZnO/Au hybrid nanoarchitectures: wet-chemical synthesis and structurally enhanced photocatalytic performance. *Environ Sci Technol* 43:8968–8973. doi:[10.1021/es902568h](https://doi.org/10.1021/es902568h)
- Wang C, Xingrong T, Shihong C, Ruo Y, Fangxin H, Dehua Y, Yun X (2012) Highly-sensitive cholesterol biosensor based on platinum-gold hybrid functionalized ZnO nanorods. *Talanta* 94:263–270. doi:[10.1016/j.talanta.2012.03.037](https://doi.org/10.1016/j.talanta.2012.03.037)
- Wang S, Huanhuan Q, Yong H, Wei D, Yijun Z, Jiafu C, Xiao H (2013) Facile one-pot synthesis of uniform TiO₂-Ag hybrid hollow spheres with enhanced photocatalytic activity. *Dalton Trans* 42:1122–1128. doi:[10.1039/C2DT32040A](https://doi.org/10.1039/C2DT32040A)
- Zeng H, Liu P, Cai W, Yang S, Xu X (2008) Controllable Pt/ZnO porous nanocages with improved photocatalytic activity. *J Phys Chem C* 112:19620–19624. doi:[10.1021/jp807309s](https://doi.org/10.1021/jp807309s)
- Zhao Y, Jiang L (2009) Hollow micro/nanomaterials with multilevel interior structures. *Adv Mater* 21:3621–3638. doi:[10.1002/adma.200803645](https://doi.org/10.1002/adma.200803645)
- Zheng Y, Chongqi C, Yingying Z, Xingyi L, Zheng Q, Kemei W, Jiefang Z (2008) Photocatalytic activity of Ag/ZnO heterostructure nanocatalyst: correlation between structure and property. *J Phys Chem C* 112:10773–10777. doi:[10.1021/jp8027275](https://doi.org/10.1021/jp8027275)
- Zhou ZY, Na T, Jun TL, Ian B, Shi GS (2011) Nanomaterials of high surface energy with exceptional properties in catalysis and energy storage. *Chem Soc Rev* 40:4167–4185. doi:[10.1039/C0CS00176G](https://doi.org/10.1039/C0CS00176G)